

Juan C. Petit · Matthias Sperl

# Structural transitions in jammed asymmetric bidisperse granular packings

May 4, 2023

**Abstract** We study the local structural changes along the jamming transitions in asymmetric bidisperse granular packings. The local structure of the packing is assessed by the contact orientational order,  $\tilde{Q}_\ell$ , that quantifies the contribution of each contact configuration (Large-Large, Small-Small, Large-Small, Small-Large) in the jammed structure. The partial values of  $\tilde{Q}_\ell$  are calculated with respect to known ordered lattices that are fixed by the size ratio,  $\delta$ , of the particles. We find that the packing undergoes a structural transition at  $\phi_J$ , manifested by a sudden jump in the partial  $\tilde{Q}_\ell$ . Each contact configuration contributes to the jammed structure in a different way, changing with  $\delta$  and concentration of small particles,  $X_S$ . The results show not only that the packing undergoes a structural change upon jamming, but also that bidisperse packings exhibit local HCP and FCC structures also found in monodisperse packings. This suggests that the jammed structure of bidisperse systems is inherently endowed with local structural order. These results are relevant in understanding how the arrangement of particles determines the strength of bidisperse granular packings.

**Keywords** Jamming transition · Structure · Amorphous · Extreme size ratio · Bidisperse packings

## 1 Introduction

The jamming transition in granular packings has been studied for years, with much attention paid to monodisperse packings since this is the simplest case [1–3]. Such a transition is defined when a set of non-contacting spheres come into contact collectively to form a rigid structure. For a monodisperse packing, the jamming transition occurs at a jamming density around  $\phi_J \approx$

0.64 in 3D. Considering a second particle size in the packing with a size ratio of  $\delta = r_S/r_L = 0.71$  and the same number of large and small particles (50:50 mixture),  $\phi_J$  increases slightly compared to the monodisperse case [2, 4, 5]. On the other hand, varying the concentration of small particles,  $X_S$ , and size ratio,  $\delta$ , studies have shown a richer jamming diagram for bidisperse packings than the monodisperse and even the 50:50 mixture with  $\delta = 0.71$  [6–15]. In this case,  $\phi_J$  shows a maximum value at a given  $X_S$  that increases as  $\delta$  decreases. Similar results have also been obtained in dense suspension where the viscosity was found to be minimal at a specific value of  $X_S$  while the jamming density was found to be maximal for the same  $X_S$  [16–20]. Such a minimal value of the viscosity also decreases whereas the maximal value of the jamming density increases when  $\delta$  decreases.

Recently, it was shown that there are critical  $\delta$  and  $X_S$  values below which the jamming structure of a bidisperse system consists only of large particles, while most small particles remain without contacts [6, 12, 14, 15]. This suggests that the jammed structure can be regarded as a monodisperse rather than a bidisperse packing, although the packing itself can still be modified by the presence of small particles at higher compression. This finding has led to reconsider the jamming transition diagram for bidisperse packings to provide a more general overview. In a recent paper, it is shown that at low  $\delta$  and low  $X_S$ , small particles can be jammed by compressing beyond the  $\phi_J$  formed by large particles [14]. Such  $\phi_J$  is extracted at a packing fraction where the fraction of large particles,  $n_L$ , contributing to the jammed structure exhibits a jump, defined by a sharp but finite value similar to that observed in the mean contact number, see Ref. [14]. A separate jump in the fraction of small particles,  $n_S$ , occurs at  $\phi > \phi_J$ , which was interpreted as the jammed transition of the small particles. This result led to the idea that a bidisperse packing in compression has two jamming transitions at low  $\delta$  and low  $X_S$ . The first jamming transition is driven by the jamming of predominantly large particles

---

Juan C. Petit · Matthias Sperl  
German Aerospace Center,  
Institute of Materials Physics in Space  
Linder Höhe, 51147 Köln,  
E-mail: Juan.Petit@dlr.de, Matthias.Sperl@dlr.de

and the second transition small particles are jammed together with large ones. This second transition was shown for  $\delta \leq 0.22$  to be an additional line extending towards higher packing densities as  $X_S$  is reduced, generalizing the jamming diagram of bidisperse packings.

The evolution of the jammed structure in a range of packing fractions has been well studied in monodisperse hard-sphere packings [21–24], showing that upon compression there is a structural transition from disordered to an ordered local structure. All works report the development of local Hexagonal Close-Packed (HCP) and Face-Centred Cubic (FCC) lattices as the system becomes denser. The evolution of the jammed structure in bidisperse packings has not been explored in detail. It is not clear how each configuration type; Large-Large (LL), Small-Small (SS), Large-Small (LS), and Small-Large (SL), contribute to the development of the jammed structure when  $\delta$  and  $X_S$  are varied. The way each particle size is packed in the system is important to understand the transition to jamming and also how such structures can lead to different structural properties. In this work, we investigate the structural evolution of jammed bidisperse packings along the first and second jamming transition lines recently reported. We will discuss that the structure factor is not a good indicator of the jamming transition, as it predicts a similar structure immediately before and at  $\phi_J$ . We will introduce the local contact orientational order (LCOR), analogous to the local bond orientational order (LBOR), as a variable sensitive to jamming that quantifies the local structures of bidisperse packings.

This paper is organized as follows. In Sec. 2, we briefly discuss the numerical simulation. We define the concentration of small particles,  $X_S$ , and discuss how the number of particles in each bidisperse mixture changes with  $X_S$ . We also explain the simulation protocol used to determine the jammed structures. Sec. 3 presents the first and second transitions for bidisperse packings. Here we present the method to obtain  $\phi_J$ . In Sec. 4, the structure factor is obtained to analyze the packing structure along the first and second transition lines. In Sec. 5, we introduce the local contact orientational order,  $\tilde{Q}_\ell$ , to quantify the local structure of the packings. Here, we investigate how  $\tilde{Q}_\ell$  changes with  $\phi$  and  $X_S$  for different  $\delta$  values. We also show results of  $\tilde{Q}_\ell$  for each configuration type to investigate their contribution to the jammed packing. Finally, we conclude with a summary and further discussion.

## 2 Numerical simulation

We perform 3D molecular dynamic simulations using MercuryDPM [25, 26] to study the role of small particles in the jammed structure of soft-sphere packings without gravity [27–29]. The absence of gravity is essential for our observations. It allows small particles to have

no contacts with the large particles and thus can undergo a collective transition upon high compression. In contrast, in the presence of gravity, small particles have already contacts with the jammed structure of large particles. These contacts make it difficult to study the contribution of small particles on the jammed structure upon compression, and as a consequence, any additional transition associated with small particles, given either by jamming density or LCOR, cannot be found. Newton’s equation for each particle is solved numerically to predict its motion in time.  $N = 6000$  particles are used to create a bidisperse packing, where a number of large,  $N_L$ , and small,  $N_S$ , particles with dimensionless radius  $r_L$  and  $r_S$  are considered. We choose the large particle radius as length scale,  $x'_u = r'_L = 1.5$ , therefore, the dimensionless radius of large particles is  $r_L = r'_L/x'_u = 1$ , while for small particles,  $r_S = r'_S/x'_u = r'_S/r'_L$ , respectively. The prime symbol represents the variable with units while the variable without prime is dimensionless. These definitions above define the size ratio as  $\delta = r'_S/r'_L = r_S \in [0.15, 1]$ . This means that any change in  $\delta$  is due to a change in the small particle size. The mass scale is chosen as  $m'_u = \rho'_p r'^3_L$ , where  $\rho'_p = 2000$  is the density of large and small particles and its dimensionless value is  $\rho_p = 1$  since  $\rho'_u = \rho'_p$ . Therefore, the dimensionless mass of the large and small particles is  $m_L = \frac{4}{3}\pi$  and  $m_S = \frac{4}{3}\pi r'^3_S = m_L \delta^3$ . The chosen time scale is  $t'_u = (m'_u/\kappa'_n)^{1/2}$  with  $\kappa'_n = 10^5$  the normal stiffness. We choose here  $\kappa_n = 1$ , since  $\kappa'_u = \kappa'_n$ . Thus  $t'_u = (\rho'_p/\kappa'_n)^{1/2} r'^{3/2}_L \approx 0.26$ . The viscous damping used is  $\gamma'_n = 1000$  and its dimensionless value is  $\gamma_n = \gamma'_n/(\rho'_u \kappa'_n r'^3_L)^{1/2} \approx 0.038$ .

The linear spring-dashpot model is used to model the contact between particles [11, 27–29]. For bidisperse packings, the effective mass,  $m_{ij}$ , the contact time,  $t_c^{ij}$ , and the coefficient of restitution,  $e_{ij}$ , depend on  $\delta$ , as can be seen in Fig. 1. Since  $e_{ij}$  depends on  $m_{ij}$  and  $t_c^{ij}$  via  $e_{ij} = \exp(-\gamma_n t_c^{ij}/2m_{ij})$ , the partial coefficients of restitution for  $\delta = 0.15$  are  $e_{LL} = 0.95$ ,  $e_{SS} = 0.48$ , and  $e_{LS} = e_{SL} = 0.60$ , see the dashed line in Fig. 1. However, as  $\delta \rightarrow 1$ ,  $e_{SS}, e_{LS} \rightarrow e_{LL}$ . This result indicates that the collisions of the SS and LS-SL configuration types are more elastic at high  $\delta$ . A background dissipation force is imposed on each particle velocity, with constant dissipation  $\gamma_b = \gamma_n$ , to damp out the kinetic energy of the particles, especially at high  $\delta$ .

A bidisperse packing formed by a given set of  $N_L$  and  $N_S$  is characterized by the size ratio  $\delta$  and the volume concentration of the small particles,  $X_S = N_S \delta^3 / (N_L + N_S \delta^3)$ . Fig. 2 shows the variation of  $N_L$  and  $N_S$  as a function of  $X_S$  for three typical values of  $\delta$ . For a fixed value of  $\delta$  the number of small particles increases while the number of large particles decreases with  $X_S$ . The intersection point, representing a packing with  $N_L = N_S = N/2$ , shifts to lower  $X_S$  values as  $\delta$  decreases. This point corresponds to the 50:50 particle mixture studied

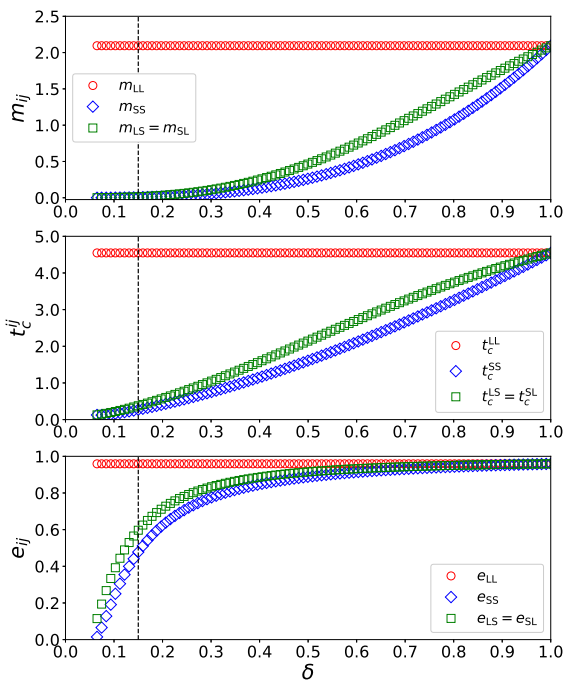


**Fig. 1** Variation of the dimensionless effective mass,  $m_{ij}$ , the dimensionless contact time,  $t_c^{ij}$ , and the partial coefficient of restitution,  $e_{ij}$ , as a function of the size ratio  $\delta$ . The dimensionless mass for each contact type is given by  $m_{LL} = 2\pi/3$ ,  $m_{SS} = m_{LL}\delta^3$ , and  $m_{LS} = m_{SL} = 2m_{LL}\delta^3/(1 + \delta^3)$ , respectively. The dimensionless contact time is determined by  $t_c^{ij} = t_c^{\prime ij}/t_u^{\prime} = \pi/(\kappa_n/m_{ij} - (\gamma_n/m_{ij})^2)^{1/2}$ . The dashed line represents the lowest value of  $\delta = 0.15$  used in this work. Note that  $e_{ij}$  stops at  $\delta \approx 0.06$  since imaginary values are obtained for  $e_{SS}$  and  $e_{LS}$  below it.

previously in bidisperse systems using  $\delta = 0.71$  [2, 4]. Far below the intersection point ( $X_S \rightarrow 0$ ), the packing is formed by small particles in a sea of large particles. As  $X_S$  increases and approaches the intersection point, the numbers of small and large particles become of the same order of magnitude. Well above the intersection point ( $X_S \rightarrow 1$ ) few large particles are embedded in a sea of small ones. This can be seen in Fig. 3 for typical bidisperse packing structures.

The initial configuration of any bidisperse packing is such that spherical particles of radius  $r_L$  and  $r_S$  are placed uniformly at random in a 3D box without gravity, allowing overlap between them, with an initial packing fraction of  $\phi_{\text{ini}} = 0.3$  and large uniform random velocities. Large overlaps lead to an initial peak in kinetic energy, but this is quickly damped by the background medium and collisions. Low density systems with high kinetic energy contribute to the rapid randomization of particles. The granular gas is then isotropically compressed to approach an initial direction-independent configuration with the target packing fraction  $\phi_0 < \phi_J$  that depends on  $\delta$  and  $X_S$ . Then a relaxation process of the system starts. Once such a process is complete, isotropic compression

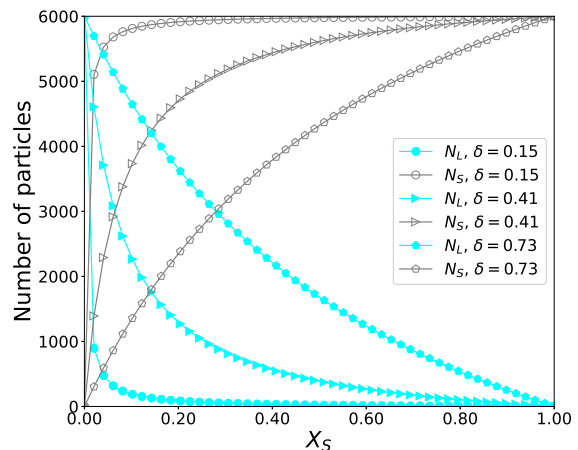
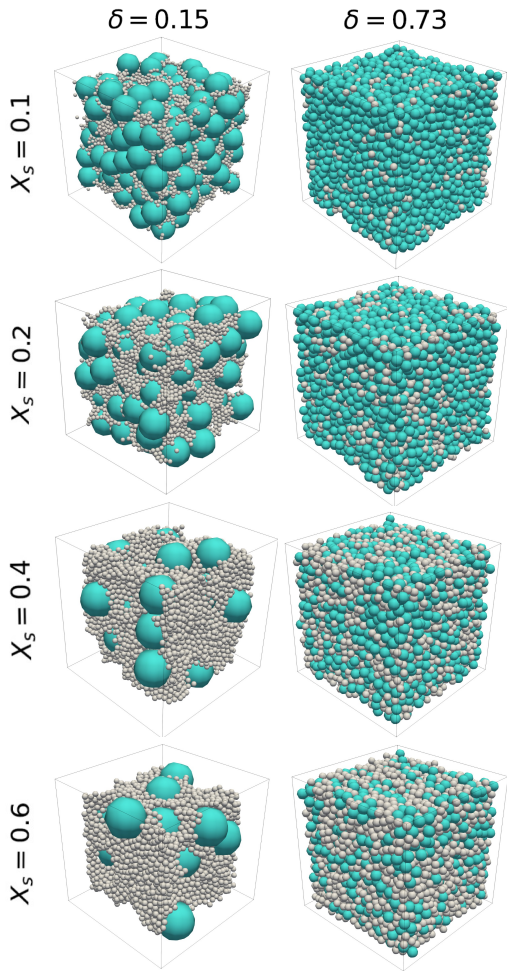


**Fig. 2** Number of large,  $N_L$ , and small,  $N_S$ , particles as a function of  $X_S$  for three typical  $\delta$ . The total number of particles is fixed at  $N = 6000$ . The intersection points represent the 50:50 mixtures at  $X_S(\delta = 0.73) \approx 0.28$ ,  $X_S(\delta = 0.41) \approx 0.06$ , and  $X_S(\delta = 0.15) = 0.01$ .

(loading) begins, which ceases when  $\phi = \phi_{\text{max}}$ . Then the isotropic decompression (unloading) process continues 10 times slower than the loading process until  $\phi_0$  is reached again. In this way, the jamming density,  $\phi_J$ , along the decompression process is obtained. Other methods of strain control could be used [2, 30, 31], but they would not have any other effects since the deformation is performed quasi-statically. After the simulation protocol is completed, the jamming density and the jammed structures of each bidisperse packing in the decompression branch are examined, since these values are less sensitive to the deformation rates [32]. A detailed discussion of the contact model and simulation procedure is given in Refs. [14, 15].

### 3 Jamming transition lines

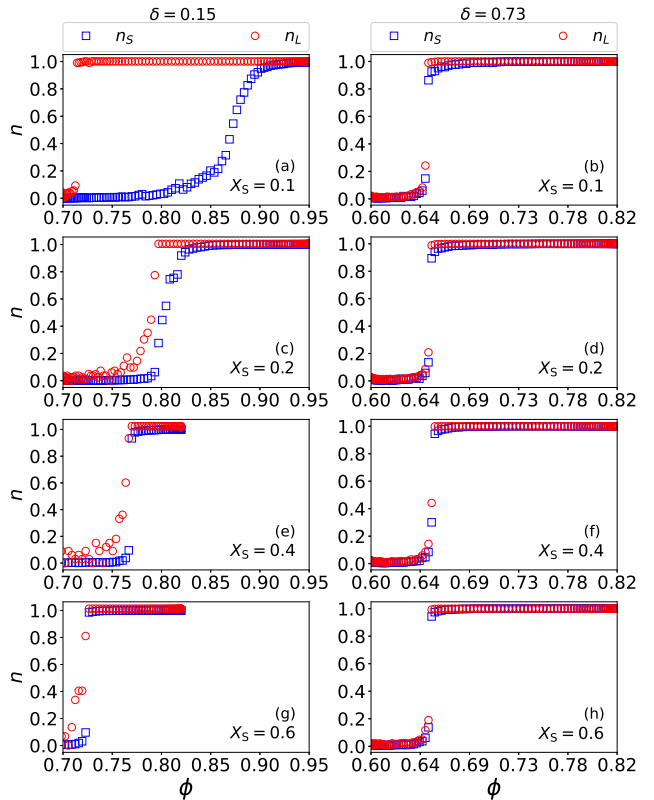
In this section, we discuss how the jamming transition is achieved for each bidisperse packing. We start by quantifying the fraction of large,  $n_L = N_L^c/N$ , and small particles,  $n_S = N_S^c/N$ , that contribute to the jammed structure as a function of  $\phi$  at different  $\delta$  and  $X_S$ .  $N_{L,S}^c$  is the number of large and small particles in contact, while  $N = N_L + N_S$  is the total number of particles in the system. Fig. 4 (right panel) shows a jump for  $\delta = 0.73$ , which represents a simultaneous contribution of both particle sizes to the jammed structure. Interestingly,  $\phi_J$  is independent of  $X_S$  showing similar values to that of a monodisperse packing,  $\phi_J^{\text{mono}} \approx 0.64$ . This finding is in line with the observation that a bidisperse packing with  $\delta = 0.73$  can be used to break up a global crystallization obtained in monodisperse packings but otherwise behaves similar to it [2, 4, 5]. Although, as we will see in Sec. 5, we still find a certain fraction of



**Fig. 3** Packing structures for two extremes  $\delta$  at different  $X_S$ . Cyan and white colors represent large and small particles, respectively. Each packing is shown at  $\phi_{\max}$ . Note that higher  $\phi$  are obtained for structures with  $\delta = 0.15$ , they are shown enlarged for better illustration. This is the reason why large particles look bigger.

local ordered structures. In contrast, a significant decoupling between  $n_L$  and  $n_S$  is obtained at lower  $X_S$  for  $\delta = 0.15$ , see Fig. 4 (a,c). Such decoupling indicates that a large number of small particles are jammed at higher densities, which corresponds to similar behavior of large particles at low densities.

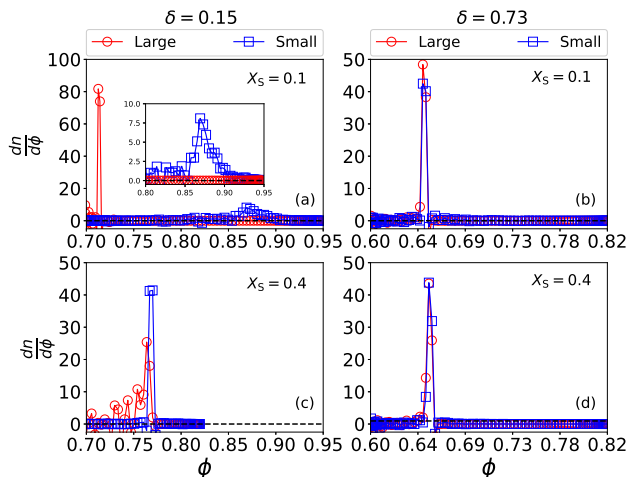
To find the exact value of the jamming density at which  $n_L$  and  $n_S$  jump as a function of  $\delta$  and  $X_S$ , we calculate the derivative  $\partial n_L / \partial \phi$  and  $\partial n_S / \partial \phi$ . We used the five-point finite difference method with an accuracy of  $\sim O(\Delta\phi^4)$  to approximate the first derivative over the data shown in Fig. 4. This method yields a value of  $\phi_J$  for both fractions of large and small particles. Fig. 5 displays the derivative of  $n_L$  and  $n_S$  as a function of  $\phi$ , showing a characteristic peak (maximum derivative) at a value consistent with  $\phi_J$ . Note that for  $\delta = 0.15$  and  $X_S = 0.1$  the peak for large particles is found at a much



**Fig. 4** Fraction of large,  $n_L$ , and small,  $n_S$ , particles in contact as a function of the packing fraction for different combinations of  $\delta$  and  $X_S$ .

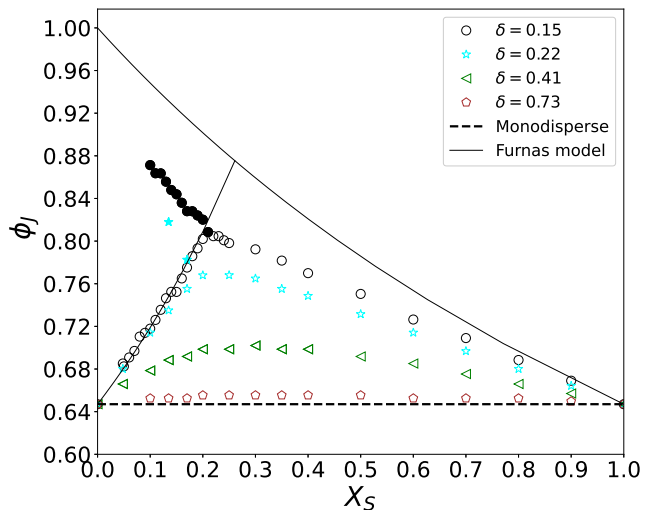
lower  $\phi$ , while a small peak is obtained at higher density for small particles, see Fig. 5 (a). The small peak in  $n_S$  is due to its smoother behavior compared to  $n_L$ . Nevertheless, a critical density can be extracted representing the largest amount of small particles jammed, see the inset in Fig. 5 (a). This proves that the system undergoes a transition from a structure with predominantly large particles to one with the participation of both particle sizes. On the other hand, at higher  $\delta$ , it becomes clear that both particle sizes contribute simultaneously to the jammed structure, see Figs. 5 (b,d). Thus, using this method, one can extract the values of  $\phi_J$  for the entire combination of  $\delta$  and  $X_S$ .

Fig. 6 shows the  $\phi_J$  values extracted by the method explained above as a function of  $X_S$  for some  $\delta$  values. For  $\delta = 0.15$ , we find that the two lines meet at  $X_S^* \approx 0.21$  with  $\phi_J \approx 0.80$ . The superscript \* indicates the concentration of small particles where the second jamming transition line emerges, see solid circles in Fig. 6. Such a point matches with the kink of the jamming lines, shifting to high  $X_S$  as  $\delta$  increases, as also reported in Ref. [6]. For  $X_S < X_S^*$ , an increasing line of densities is observed for small  $\delta$  as  $X_S \rightarrow 0$ . Such a line is an extension of the transition where both large and small particles are jammed, having a particle mean overlap less than 1% of the large par-



**Fig. 5** Derivative of  $n_L$  and  $n_S$  as a function of the packing fraction for  $\delta = 0.15$  and  $\delta = 0.73$  at different  $X_S$ . The maximum value of each derivative is considered as the jamming density of each particle size. The inset is a zoom-in of the maximum derivative of  $n_S$ .

ticle radius, see Ref. [15]. The values of  $\phi_J$  are compared with a model introduced by Furnas almost a century ago [33] to predict the highest density of aggregates used in the production of mortar and concrete. This model states that  $\phi_J$  can decouple at an extreme particle size ratio ( $\delta \rightarrow 0$ ) into two limits that have a common point at  $X_S^*$ . The lower limit considers an approximation where large particles dominate the jammed structure, while small particles are not considered because their number is not sufficient to play a role ( $0 \leq X_S < X_S^*$ ). Thus, the jamming density is given by  $\phi_J(X_S) = \phi_J^{\text{mono}}/(1 - X_S)$ . The upper limit, both large and small particles participate in the jammed structure ( $0 \leq X_S \leq 1$ ). In this case, the number of small particles is large enough to drive some large particles into the jammed state. Therefore,  $\phi_J$  is written by  $\phi_J(X_S) = \phi_J^{\text{mono}}/(\phi_J^{\text{mono}} + (1 - \phi_J^{\text{mono}})X_S)$ . The Furnas model describes the trend of the data by following the values for low  $X_S$  corresponding to the first jamming state. It shows a maximum density of  $\phi_J(X_S^*) \approx 0.87$  at  $X_S^* = (1 - \phi_J^{\text{mono}})/(2 - \phi_J^{\text{mono}}) \approx 0.26$ , which is in reasonable agreement with the value obtained here for  $X_S^* \approx 0.21$  at  $\delta = 0.15$ . The model also shows an additional transition line emerging where the two limits meet and end at a density of one. Such an additional line has not been considered in previous works when using the Furnas model, see Refs. [6, 7, 9, 10]. The additional line resulting from our simulation data qualitatively follows the Furnas prediction and ends at  $X_S^{\circ} = 0.1$  for the lowest  $\delta$ , see Fig. 6. The superscript  $\circ$  marks the endpoint of the extension line. The transition line ends at  $X_S^{\circ}$  since there is no jump in  $n_S$  for  $X_S < X_S^{\circ}$ , but rather this quantity increases continuously in this region and does not exhibit any features of a jump transition. This allows us to argue that the additional transition line



**Fig. 6** Jamming density,  $\phi_J$ , as a function of the concentration of small particles,  $X_S$ , for different values of the size ratio,  $\delta$ . The extreme  $X_S$  values (0 and 1) correspond to monodisperse systems, which have a value of  $\phi_J^{\text{mono}} \approx 0.64$ , indicated by the dashed horizontal line. The solid lines represent the Furnas model [33], see the text for its explanation and ideas. Open (solid) symbols represent the first (second) transition lines.

terminates in an endpoint at a finite  $X_S^{\circ}$  that depends on  $\delta$ , see Ref. [14].

The jamming transition lines observed in Fig. 6 represent a more complete jamming diagram for bidisperse packings. Indeed, the second transition starts at a size ratio around  $\delta = 0.22$  and becomes longer for smaller  $\delta$ . This particular value of  $\delta$  coincides with the minimum size ratio,  $\delta_{\text{min}} \approx 0.225$ , at which a small particle can fit into the gap left by large particles forming a tetrahedral structure, see Ref. [11]. For  $\delta > \delta_{\text{min}}$ , a small particle cannot fit into the gap left by the large particles in contact, destroying the tetrahedral structure and creating different local structures. For  $\delta < \delta_{\text{min}}$ , the small particle is too small to fit into the gap of the tetrahedral becoming a rattler in a system. Instead, a number of small particles are now needed to fill the gap in order to come in contact with large particles. In this case, other local structures are developed. This will be discussed in Sec. 5.

So far, we have shown the dependence of  $\phi_J$  on  $\delta$  and  $X_S$ .  $\phi_J$  is enhanced for  $\delta < 0.73$ , especially at very low  $\delta$  and low  $X_S$ , showing a second transition. The differences in jamming densities between the extreme size ratios are remarkable. For example, one would have expected a substantial variation of  $\phi_J$  for  $\delta = 0.73$ , since this is far from the monodisperse case of only large,  $\delta = 0$ , and only small particles,  $\delta = 1$ . Instead,  $\phi_J$  appears to be constant for  $\delta = 0.73$  and hardly varies above  $\phi_J^{\text{mono}}$  independent of  $X_S$ . This means that packings with  $\delta > 0.73$  would have  $\phi_J$  values close to  $\phi_J^{\text{mono}}$  and probably similar properties as a monodis-

perse packing. Examining the jammed structure of the packings as a function of  $\delta$  and  $X_S$  may provide better insight into the values of  $\phi_J$  for  $\delta = 0.73$ . In addition, it is important to understand how the jammed structure evolves as the system approaches jamming and how it changes along the first and second jamming transitions. The following sections are devoted to the study of the structure of jammed bidisperse packings along the jamming transition lines.

#### 4 Structure factor analysis

To understand how the structure of a bidisperse packing changes with  $X_S$  and  $\delta$ , we calculate the total and partial structure factors,  $S(q)$ , at  $\phi_J$ . This allows exploring the structural contribution that each configuration type has in the jammed packing. A general definition of the partial  $S(q)$  is

$$S_{\nu\beta}(q) = \frac{1}{N} \sum_{i=1}^{N_\nu} \sum_{j=1}^{N_\beta} \cos(\mathbf{q} \cdot \mathbf{r}_\nu^i) \cos(\mathbf{q} \cdot \mathbf{r}_\beta^j) + \frac{1}{N} \sum_{i=1}^{N_\nu} \sum_{j=1}^{N_\beta} \sin(\mathbf{q} \cdot \mathbf{r}_\nu^i) \sin(\mathbf{q} \cdot \mathbf{r}_\beta^j) \quad (1)$$

where  $\nu, \beta \in \{L, S\}$  and the sum runs over all  $\nu$  and  $\beta$  particles. Therefore, the total  $S(q)$  can be decomposed in terms of configuration types:  $S_{LL}(q)$ ,  $S_{SS}(q)$ ,  $S_{LS}(q)$ , and  $S_{SL}(q)$  as shown in Ref. [34]. By symmetry, we obtain that  $S_{LS}(q) = S_{SL}(q)$ . Thus, we show the structure factor of only one term and call it  $S_{\text{mix}}(q)$ . The term ‘‘mix’’ is only used in this section to highlight the equivalence of  $S(q)$  for SL and LS. As we will explain in Sec. 5, SL and LS contact configurations are differently treated when calculating LCOR, thus the term ‘‘mix’’ is no longer used. Therefore, the total structure factor is then written as  $S(q) = S_{LL}(q) + S_{SS}(q) + 2S_{\text{mix}}(q)$ .

Fig. 7 shows the total and partial structure factors at jamming for  $\delta = 0.73$  at different  $X_S$ . We obtain that LL dominates over SS and mix configurations for the lowest  $X_S$ , see Figs. 7 (b)-(d). As  $X_S$  increases, SS begins to dominate the structure over the other configuration types. This is evident as the number of small particles increases with  $X_S$ . The exchange of the configuration type in the dominance of the packing structure marks a structural change above a certain  $X_S$ . We think that this occurs at  $X_S(\delta = 0.73) \sim 0.28$  since it corresponds to the 50:50 particle mixture of the packing, see Fig. 2. On the other hand,  $S_{\text{mix}}(q)$  appears to be independent of  $X_S$ , suggesting that it has no effect on the overall structure factor. The meaning of the negative value in  $S_{\text{mix}}(q)$  indicates anticorrelated density fluctuations between small and large particles at long distances ( $q \rightarrow 0$ ), i.e., high density fluctuations of small particles correspond to low density fluctuation of

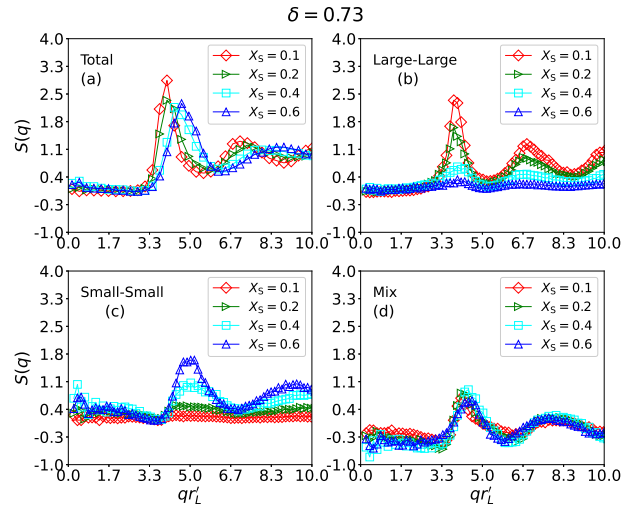


**Fig. 7**  $S(q)$  vs  $qr'_L$  at  $\phi_J$  for  $\delta = 0.73$  at different  $X_S$ .  $S(q)$  of (a) Total, (b) Large-Large, (c) Small-Small, and (d) Mixed particle configurations.

large ones. For positive values, the density fluctuations of large and small particles need to be mostly in sync and so are correlated.

The total  $S(q)$  shows a gradual change due to the structural transition that the LL and SS configurations undergo, causing the system to explore different local structures as  $X_S$  varies. Despite  $S_{LL}(q)$  and  $S_{SS}(q)$  show a significant change with  $X_S$ , the whole  $S(q)$  shows similar structure factors, i.e., similar jammed structures are obtained where their peaks become wider and shifted for high  $q$  as  $X_S \rightarrow 1$ . We think that the similar structures might be responsible for the similar jamming densities observed in Fig. 6 for  $\delta = 0.73$ . This indicates that the packing structure influences the jamming density, as it was recently shown in Ref. [35], where the random close packing in monodisperse packings can be theoretically calculated by considering only specific local disorder arrangements of particles.

For  $\delta = 0.15$ , the structure factor is different from  $\delta = 0.73$ . At the first transition, the total  $S(q)$  is given by  $S_{LL}(q)$  since the jammed structure consists only of large particles (data not shown). On the other hand, at the second transition, both large and small particles are jammed. The total  $S(q)$  is dominated by SS over LL and mix configurations types, see the magnitude of the y-axis of Figs. 8 (b)-(d). This dominance rises as  $X_S$  increases, leading to a packing structure formed mostly of small particles with some contribution from mix configurations, see Fig. 8 (d). The peaks shown by  $S_{SS}(q)$  at long wavelengths ( $q \lesssim 3.3$ ), see Fig. 8 (c), can be due to (i) the formation of ordered regions between small particles, which is possible because there are many more small particles than large ones and (ii) high density fluctuations of small particles compared to large ones. Few

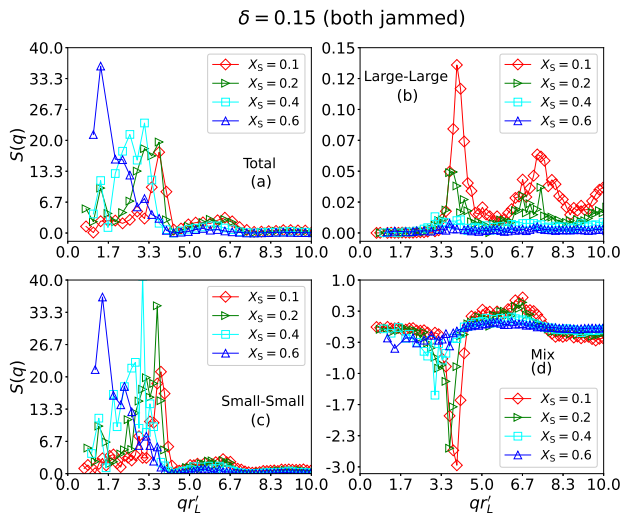


**Fig. 8**  $S(q)$  vs  $qr'_L$  for  $\delta = 0.15$  at different  $X_S$  along the transition line where both species are jammed.  $S(q)$  of (a) Total, (b) Large-Large, (c) Small-Small and (d) Mixed particle configurations.

large particles are surrounded by many small ones at large scales. This is also observed in Fig. 8 (d), where a huge disparity between large and small particle number at a large distance gives rise to negative values in  $S_{LS}(q)$ , leading to anticorrelated density fluctuations.

Fig. 9 shows the variation of total and partial  $S(q)$  before, at the first and at the second jamming transition for  $\delta = 0.15$  at  $X_S = 0.1$ . The  $S(q)$  shown at the first and second transitions differ as a consequence of further compression, which causes small particles to jam with the jammed structure of large particles and to form high crystallized regions of small particles, see the peaks in Fig. 9 (a,c) and particle configurations in Fig. 3. However, it is difficult to interpret such a difference as an indication of a jammed transition. On the other hand, the  $S(q)$  immediately before and at the first jamming transition are identical to each other, which could be interpreted as the same packing structure. Note that the difference in the packing fraction between the structure before and the structure at the first jamming transition is  $\Delta\phi \approx 10^{-3}$ . This small value does not make much difference between the total and partial  $S(q)$  when going from a loose to the first jamming state. The reason for this is that all particles in the system are used to calculate the structure factor, regardless of whether the particles are in contact or not. This makes it difficult to distinguish whether the structure is present before, at the first, or even at the second jamming transition. In the next section, we will introduce and examine a sensitive variable that can distinguish the structural features of a jamming transition.

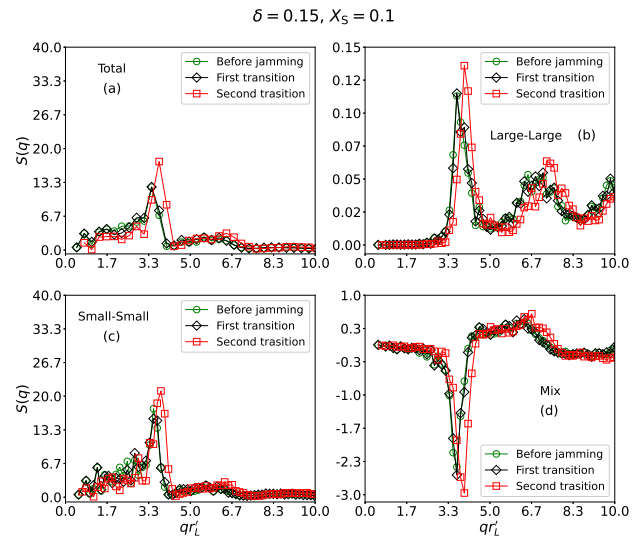


**Fig. 9** Comparison of  $S(q)$  before ( $\phi = 0.7143$ ), at the first ( $\phi_J = 0.7160$ ) and second jamming transition ( $\phi_J = 0.8712$ ) for  $\delta = 0.15$  at  $X_S = 0.1$ .  $S(q)$  of (a) Total, (b) Large-Large, (c) Small-Small, and (d) Mixed particle configurations.

## 5 Local contact orientational order $\tilde{Q}_\ell$

In the previous section, we showed that  $S(q)$  before jamming is identical to  $S(q)$  at the first transition, suggesting that there is no difference in structure between them. As  $\phi \rightarrow \phi_J$ , a loose granular packing with a non-contacting structure approaches the jamming state. At  $\phi = \phi_J$ , the packing undergoes a structural transition defined as a jammed structure, which is not accounted for by the structure factor. To understand the evolution of a jammed structure, and even more to distinguish the structures along the first and second transitions given in Fig. 6, a variable sensitive to each structural feature at jamming is needed. This section is dedicated to the introduction of a variable that is not only able to predict structural changes in the packing, but also to quantify the contribution of specific local structures formed by each configuration type in the jammed structure.

### 5.1 Definition of $\tilde{Q}_\ell$

A variable that has been used to study the structure and measure crystallinity in supercooled liquids and metallic glasses is the bond orientational order (BOR),  $Q_\ell$ , see Ref. [36]. It is determined by summing the spherical harmonics of degree  $\ell$  of all bonds in the system. Here, a bond is defined by the connection of each particle center  $i$  with the center of its nearest neighbors  $j$ . A local measure of this variable,  $Q_{\ell, \text{local}}$ , was proposed in Refs. [36, 37] as a more accurate measure for identifying local structures. It determines the BOR on each

particle and then is averaged over all particles. However,  $Q_{\ell,\text{local}}$  depends on the method used for nearest neighbor detection. For instance, the radial distribution function with a cutoff  $r_{\text{max}}$  is used [36, 38, 39], however, it leads to different  $Q_{\ell,\text{local}}$  values when  $r_{\text{max}}$  is varied. Delauney triangulation method [37, 40], morphometric neighbourhood [41] and an extension of the morphometric neighborhood applied to noisy structures [42] has also been applied for identifying nearest neighbors. Due to neighborhood ambiguity,  $Q_{\ell,\text{local}}$  is not uniquely defined. Here, we introduce an alternative definition of the bond orientational order. Instead of using a special detection method to find the nearest neighbors, we use the contacts between particles to define the *local contact orientational order* (LCOR),  $\tilde{Q}_\ell$ . In this way, the neighbors of a particle  $i$  are already defined by their contacts. The definition of  $\tilde{Q}_\ell$  states that before jamming when no jammed structure has yet formed, zero values of  $\tilde{Q}_\ell$  must be obtained. However, there is a possibility that an isolated accumulation of contact particles will yield a nonzero but low value of  $\tilde{Q}_\ell$ . Therefore, LCOR abandons the definition of a recent work [43], in which the local bond orientational order at jamming is zero for highly amorphous packings. In our work, amorphous packings are characterized by the onset of the jamming structure where  $\tilde{Q}_\ell$  is not necessarily zero but has a finite low value. While high values of  $\tilde{Q}_\ell$  represent an ordered packing. For dense packings where  $\phi \gg \phi_J$ , we expect BOR to be equal to LCOR,  $Q_{\ell,\text{local}} = \tilde{Q}_\ell$ , since the detection method used in BOR can already identify those  $j$  particles in contact with  $i$  particle as nearest neighbors.

The local contact orientational order is then calculated by

$$\tilde{Q}_\ell = \frac{1}{N} \sum_{i=1}^N \left( \frac{4\pi}{2\ell+1} \sum_{m=-\ell}^{\ell} \left| \frac{1}{N_c^i} \sum_{j=1}^{N_c^i} Y_{\ell m}(\theta_j, \varphi_j) \right|^2 \right)^{1/2}, \quad (2)$$

where  $Y_{\ell m}(\theta_j, \varphi_j)$  is the spherical harmonics of degree  $\ell$  and of order  $m$ ,  $\theta_j$  and  $\varphi_j$  are the polar and azimuthal angles formed by  $i$  particle center between their  $j$  contacts with respect to the  $z$  and  $x$  axes, respectively.  $N_c^i$  is the number of contacts of  $i$  particle and  $N$  is the total number of particles.

## 5.2 Frequency distribution of $\tilde{Q}_6$

To get a first insight into the structures of the jammed bidisperse granular packings, we determine  $\tilde{Q}_6$  for each particle  $i$  in the system. In this way, we can distinguish the LCOR of large particles from that of small particles. The reason for calculating  $\tilde{Q}_6$  is because it can be used to quantify possible six-fold local crystal structures that form between particles of the same size. For example, it has been shown that the packing structure of particles

of one size tends to form local HCP and FCC structures upon compression, becoming more frequent for denser packings [21–24]. In particular, the distribution of the bond orientational order shows characteristic peaks at  $\tilde{Q}_6^{\text{HCP}} = Q_{6,\text{local}}^{\text{HCP}} = 0.48$  and  $\tilde{Q}_6^{\text{FCC}} = Q_{6,\text{local}}^{\text{FCC}} = 0.57$ , consistent with the dominance of local HCP and FCC structures [22–24]. Here, we assume that LCOR must exactly match with BOR for HCP and FCC structures. With this background, we can study how large and small particles are packed according to a six-fold lattice as a function of  $\delta$  and  $X_S$ .

The values of  $\tilde{Q}_6$  for large and small particles are used to construct independent frequency distributions,  $P(\tilde{Q}_6)$ . Such distribution is shown in Fig. 10 (a, b) at  $\phi_J$  for  $\delta = 0.73$  at two relevant  $X_S$  values.  $P(\tilde{Q}_6)$  expresses the population of large and small particles with  $\tilde{Q}_6$  within the jammed structure. In general, the distributions follow a Gaussian-like behavior, with their mean value depending on the particle size. For  $X_S = 0.4$  the structure is dominated by small particles, while for  $X_S = 0.1$  the large particles predominate. In both cases,  $P(\tilde{Q}_6)$  exhibits a fraction of local HCP and FCC structures formed by both large and small particles that change with  $X_S$ , see the dashed and dotted lines in Figs. 10 (a, b). For  $\delta = 0.15$  a similar explanation can be given, but in this case, small particles always dominate the jammed structure over large ones, see Figs. 11 (a, b). At  $X_S = 0.1$ , the system undergoes several jamming transitions during compression. The first jamming transition is caused by large particles at  $\phi_J \approx 0.71$ , where  $P(\tilde{Q}_6)$  is indicated in the inset of Fig. 11 (a). This shows that the packing is not fully ordered despite the formation of some local HCP and FCC structures. Instead, it shows a wide range of local structures. At the second transition,  $\phi_J \approx 0.87$ , the small particles dominate the jammed structure since they disrupt the jammed structure of large ones resulting in less contacts of LL, giving rise to  $0.2 \leq \tilde{Q}_6 \leq 0.3$ . As  $X_S$  increases, large particles are less present in the system, leading to a monodisperse packing of small particles. Fig. 11 (b) shows this scenario, where the mean of the distribution coincides with  $\tilde{Q}_6^{\text{HCP}}$ , indicating that most small particles form hexagonal local structures. We also find that the population of local HCP and FCC structures increases with  $X_S$ , suggesting that the local order of the packing increases with the concentration of small particles.

For a deeper understanding of the local structure, the configuration of large and small particles at jamming are separately depicted using dots with specific colors. Each dot is placed at each particle center while its color represents the value of  $\tilde{Q}_6$  of the particle. Dark colors represent the local disordered surrounding of the particles, while light colors correspond to the local ordered ones. Although this representation does not allow to see a particular structural lattice, it allows to distinguish the local arrangement around each  $i$  particle,

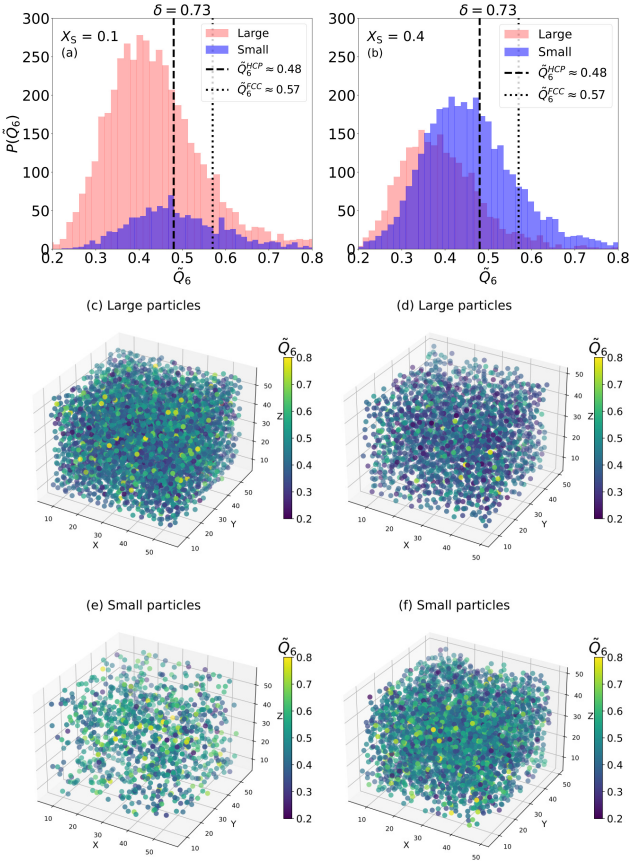


**Fig. 10** Frequency distribution,  $P(\tilde{Q}_6)$ , of large and small particles at  $\phi_J$  for  $\delta = 0.73$  at (a)  $X_S = 0.1$  and (b)  $X_S = 0.4$ . The dashed and dotted lines represent  $\tilde{Q}_6^{\text{HCP}} = 0.48$  and  $\tilde{Q}_6^{\text{FCC}} = 0.57$ , respectively. (c)-(f) Configurations of large and small particles at  $\phi_J$ . Each dot represents the center of a particle and the color indicates the magnitude of  $\tilde{Q}_6$ . The lowest value of  $\tilde{Q}_6$  (dark color) represents a disordered lattice, while the highest value (light color) is an ordered one. The dots are barely transparent to reveal the structure behind them.

and also how  $\tilde{Q}_6$  is distributed in the jammed structure. Fig. 10 (c)-(f) shows the distribution of  $\tilde{Q}_6$  in the jammed packing for  $\delta = 0.73$ . Looking at Fig. 10 (c) and Fig. 10 (f), where large and small particles dominate the structure at different  $X_S$ , one cannot see much difference between the distributions of  $\tilde{Q}_6$ . This indicates that similar structures are obtained independently of  $X_S$ , thus leading to similar  $\phi_J$ , see Fig. 6. For  $\delta = 0.15$ , the distribution of  $\tilde{Q}_6$  shows a different scenario with  $X_S$ . At  $X_S = 0.4$ , the distribution of  $\tilde{Q}_6$  is dominated by small particles, see Fig. 11 (f), while large ones do not contribute between  $0.2 \leq \tilde{Q}_6 \leq 0.8$ , see Fig. 11 (d). This happens due to the low number of large particles in the system,  $N_L \approx 32$ . Thus, they tend to share only contacts with small particles. This leads to  $\tilde{Q}_6 < 0.2$  for large particles. For  $X_S = 0.1$  and second transition, small particles still dominate the distribution of

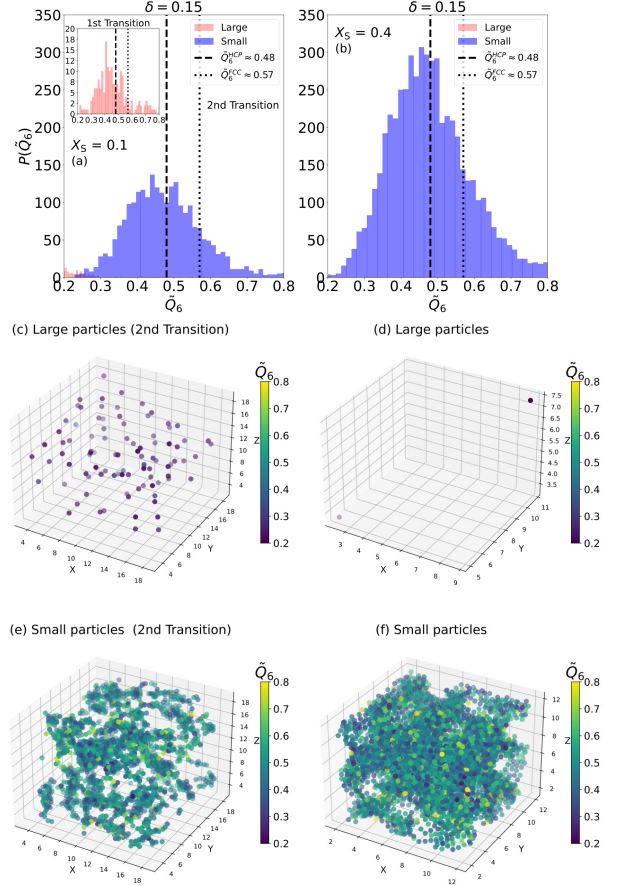


**Fig. 11** Frequency distribution,  $P(\tilde{Q}_6)$ , of large and small particles at  $\phi_J$  for  $\delta = 0.15$  at (a)  $X_S = 0.1$  at the second transition and (b)  $X_S = 0.4$ . The dashed and dotted lines represent  $\tilde{Q}_6^{\text{HCP}} = 0.48$  and  $\tilde{Q}_6^{\text{FCC}} = 0.57$ , respectively. The inset in (a) represents  $P(\tilde{Q}_6)$  at the first jamming transition. (c)-(f) Configurations of large and small particles at  $\phi_J$ . Each dot represents the center of a particle and the color indicates the magnitude of  $\tilde{Q}_6$ . The lowest value of  $\tilde{Q}_6$  (dark color) represents a disordered lattice, while the highest value (light color) is an ordered one. The dots are barely transparent to reveal the structure behind them.

$\tilde{Q}_6$  over large ones, see Fig. 11 (c, e). In this case, the distribution of  $\tilde{Q}_6$  shows a structure where small particles form clusters of the same  $\tilde{Q}_6$  value (specifically between  $\tilde{Q}_6^{\text{HCP}} = 0.48$  and  $\tilde{Q}_6^{\text{FCC}} = 0.57$ ). This indicates that small particles accumulate in HCP and FCC structures.

The results presented above show that bidisperse packings not only form HCP and FCC crystal-like structures of the same particle size, but also other local structures are relevant in the packing. In addition to Large-Large and Small-Small particle contacts lead to specific local structures, contacts between large and small particles also tend to form completely different ones. Such local structures are already accounted for in the distribution of  $P(\tilde{Q}_6)$ , but are difficult to distinguish from the six-fold lattice. To explore the different local structures,

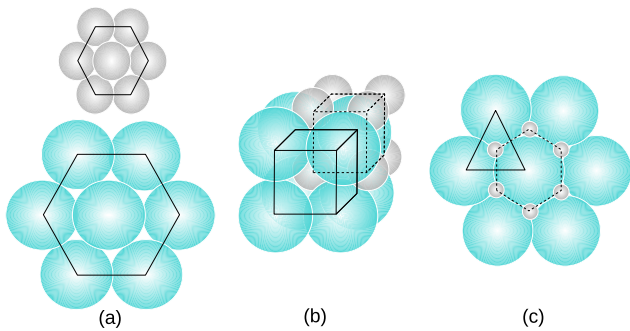


**Fig. 12** Illustration of typical structures found in bidisperse packings. (a) Hexagonal structures are generally formed by LL and SS contact configurations. (b) For  $\delta = 0.73$ , the densest lattice is a cubic structure formed between LS (dashed line) and SL particle contacts (solid line). (c) For  $\delta = 0.15$ , triangular and hexagonal lattices are formed between SL (solid line) and LS particle contacts (dashed line) to achieve the most efficient lattice.

in the next section we will investigate how the individual structures of the contact configuration contribute to the jammed structure of the bidisperse packings.

### 5.3 Partial $\tilde{Q}_\ell$ of local structures

$\tilde{Q}_\ell$  is determined for each contact configuration: LL, SS, SL, and LS. For LL and SS, we determined  $\tilde{Q}_6$  because they can form local hexagonal structures when are packed, see Fig. 12 (a). Mixed contacts are treated differently. Large particles can be packed with small particles in different ways, depending on the size ratio, see Ref. [11]. For  $\delta = 0.73$ , one can demonstrate that the most efficient lattice is a cubic lattice, where a small (large) particle with radius  $r_S = (\sqrt{3} - 1)r_L$  is in the center of a cube of large (small) particles, see Fig. 12 (b). Thus, we calculate  $\tilde{Q}_8$  for SL and LS, respectively. For  $\delta = 0.15$ , a small particle with radius  $r_S = [(\sqrt{3} - 1)/2\sqrt{3}]r_L$  fits into a triangular lattice of large particles, while a large particle fits into a hexagonal lattice of small ones, Fig. 12 (c). Therefore, we use  $\tilde{Q}_3$  for SL and  $\tilde{Q}_6$  for LS. In this way, we get a better approximation of how each contact configuration assembles and contributes as the system approaches jamming, and also along the first and second jamming transitions.

Other  $\tilde{Q}_\ell$  values can also be calculated on LL and SS contact configurations. For example,  $\tilde{Q}_4$  and  $\tilde{Q}_8$  can be determined to account for square and cubic local structures. However, we restrict ourselves to  $\tilde{Q}_6$  since LL and SS tend to form six-fold lattices, HCP and FCC, which are the densest lattices. For the mixed contact configurations,  $\tilde{Q}_\ell$  is determined by  $\delta$  since it leads to the densest lattice formed between large and small particles, see Fig. 12.

Fig. 13 shows the values of partial  $\tilde{Q}_6^{LL}$ ,  $\tilde{Q}_6^{SS}$ ,  $\tilde{Q}_8^{LS}$  and  $\tilde{Q}_8^{SL}$  as a function of  $\phi$  for  $\delta = 0.73$  at different  $X_S$ .

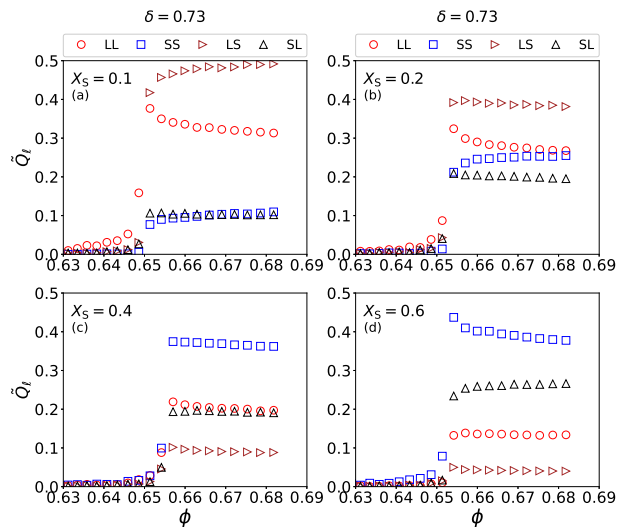


**Fig. 13** Partial  $\tilde{Q}_\ell$  vs  $\phi$  for  $\delta = 0.73$  at different  $X_S$ .  $\tilde{Q}_6$  is calculated for LL and SS contacts as they can form six-fold HCP and FCC structures. While  $\tilde{Q}_8$  is used for LS and SL contacts since a cubic structure is the densest lattice. The jamming densities at each jump correspond to  $\phi_J(X_S = 0.1) = 0.647$ ,  $\phi_J(X_S = 0.2) = 0.653$ ,  $\phi_J(X_S = 0.4) = 0.655$  and  $\phi_J(X_S = 0.6) = 0.653$ .

We find that all partial  $\tilde{Q}_\ell$  have similar density, namely  $\phi_J \approx 0.65$ , independent of  $X_S$ . This agrees with the results shown in Fig. 4, where the fraction of large,  $n_L$ , and small particles,  $n_S$ , show a jump at the same  $\phi_J$ . However, a clear difference in the structural arrangement of the contact configurations is observed when  $X_S$  changes. For  $X_S = 0.6$ ,  $\tilde{Q}_6^{SS}$  dominates the jammed structure compared to  $\tilde{Q}_6^{LL}$ , indicating the formation of a fraction of six-fold structures in the system, see Fig. 13 (d).  $\tilde{Q}_8^{SL}$  dominates next the jammed structure over  $\tilde{Q}_8^{LS}$  showing that there are higher local formations of cubic structures in which small particles are surrounded by large ones. When  $X_S$  decreases, the dominance of SS and SL in the jammed structure is completely exchanged by LL and LS, see Fig. 13 (a). This change in structural dominance, indicated by  $\tilde{Q}_\ell$ , is due to the high number of large particles present at low  $X_S$  that tends to form local six-fold and cubic structures, see Fig. 12 (b). One can speculate that there should be a certain value of  $X_S$  at which all partial  $\tilde{Q}_\ell$  are equal. For  $\delta = 0.73$ , this could be at  $X_S = 0.28$ , which corresponds to the 50:50 mixture, see Fig. 2. However, this needs to be investigated and clarified in future work.

For  $\delta = 0.15$  the scenario is different.  $\tilde{Q}_6^{SS}$  and  $\tilde{Q}_3^{SL}$  always dominate the jammed structure over  $\tilde{Q}_6^{LL}$  and  $\tilde{Q}_6^{LS}$  due to the low number of large particles. We note that for  $X_S > 0.2$  the partial  $\tilde{Q}_\ell$  jumps at the same  $\phi_J$ . This suggests that some HCP, FCC, and triangular structures are formed during jamming, which become more frequent as  $\phi$  increases. For  $X_S < 0.2$ , there is

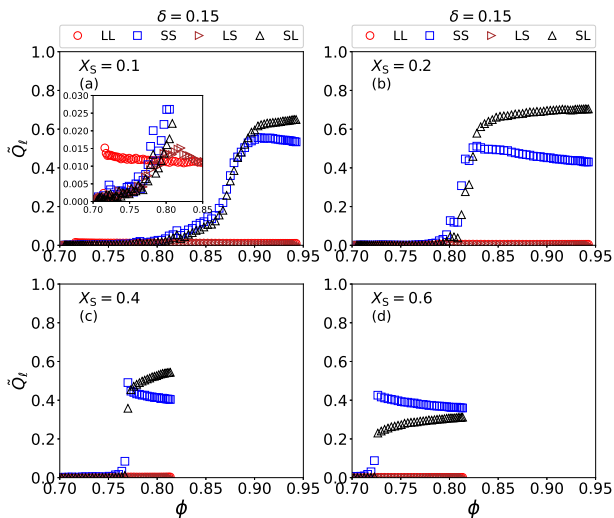


**Fig. 14** Partial  $\tilde{Q}_\ell$  vs  $\phi$  for  $\delta = 0.15$  at different  $X_S$ .  $\tilde{Q}_6$  is calculated for LL and SS contacts as they can form six-fold HCP and FCC structures. While  $\tilde{Q}_6$  and  $\tilde{Q}_3$  are used for LS and SL contacts, respectively. Each jamming density occurs at  $\phi_J^L(X_S = 0.1) = 0.717$  and  $\phi_J^S(X_S = 0.1) = 0.871$ .  $\phi_J^L(X_S = 0.2) = 0.804$  and  $\phi_J^S(X_S = 0.2) = 0.820$ .  $\phi_J(X_S = 0.4) = 0.769$  and  $\phi_J(X_S = 0.6) = 0.726$ . The superscripts L and S in  $\phi_J$  represent the jamming of large and small particles at different densities. The inset shows the rising point of each contact type contribution at low  $\phi$ .

a structural decoupling in the packing depending on the contact configurations, becoming more evident for  $X_S = 0.1$ . A first jump is observed at  $\phi_J \approx 0.71$  which indicates the first jamming transition of the system. An amorphous structure with low formation of six-fold structures is obtained with  $\tilde{Q}_6^{LL} \approx 0.015$ , see the inset in Fig. 14 (a). Upon further compression, small particles begin to contribute to the jammed structure. This is indicated by the smooth increase in  $\tilde{Q}_6^{SS}$ ,  $\tilde{Q}_6^{LS}$ , and  $\tilde{Q}_3^{SL}$ . Then, the structure is dominated by SS and SL contact configurations at  $\phi \approx 0.77$ . At the second transition,  $\phi_J \approx 0.87$ , where a large number of small particles suddenly jam, we find that  $\tilde{Q}_6^{SS} \approx 0.28$ , which is far from the typical values found in the local HCP and FCC packing structures. One can assume that the structure is disordered but endowed with a local order due to the existence of a fraction of HCP and FCC structures, see Fig. 11 (a).

Fig. 13 and Fig. 14 display an unusual behavior of  $\tilde{Q}_\ell$  for  $\phi \gg \phi_J$ :  $\tilde{Q}_\ell$  decreases or increases with  $\phi$  depending on the contact type. We think that this behavior is a consequence of over-compression of the system that generally leads to different particle penetrations and distortion of the packing structure. For a full discussion of the contact type penetration as a function of  $\phi$ , see Ref. [15].

## 6 Summary and conclusion

We have studied the structural transition along the first and second jamming transition lines in bidisperse granular packings. The local contact orientational order (LCOR),  $\tilde{Q}_\ell$ , was introduced to quantify the local structures of the packings by considering particle contacts as nearest neighbors. This means that any sudden change in contacts will be reflected on  $\tilde{Q}_\ell$ . The global structure of each bidisperse packing was divided into contact configurations, i.e., Large-Large (LL), Small-Small (SS), Large-Small (LS), and Small-Large (SL), to quantify the role of each contact configuration in the jammed packing. For the LL and SS contact configurations,  $\tilde{Q}_6$  was calculated with respect to the six-fold lattice, while LS and SL were treated differently because the local structures depend on  $\delta$ . For  $\delta = 0.73$ ,  $\tilde{Q}_8$  was determined for LS and SL because a cubic lattice is the most efficient one. For  $\delta = 0.15$ ,  $\tilde{Q}_3$  and  $\tilde{Q}_6$  were calculated for SL and LS since they tend to form triangular and hexagonal lattices, respectively.

We found that for  $\delta = 0.73$  all partial  $\tilde{Q}_\ell$  show a sudden jump at the same  $\phi_J$ , but have different contributions as  $X_S$  changes. For example, at  $X_S = 0.1$ , the jammed structure is dominated by a fraction of six-fold and cubic lattices of LL and LS, respectively. In contrast, for  $X_S = 0.6$ , this scenario is dominated by the same local structures, but for SS and SL contact configurations. For  $\delta = 0.15$ , a different behavior is observed. For  $X_S = 0.1$ , the contribution of each contact configuration to the jammed structure decouples as  $\phi \rightarrow \phi_J$ . At  $\phi_J \approx 0.71$ ,  $\tilde{Q}_6^{LL}$  shows a jump to a very low value, while the rest of the partial  $\tilde{Q}_\ell$  are zero. This represents the formation of an amorphous jammed structure and thus the first jamming transition of the system. Upon further compression, we observe a structural change experienced by small particles, marking the second jamming transition. The jammed structure at the second transition is dominated by a fraction of six-fold and triangular lattices of SS and SL contact configurations. For  $X_S > 0.2$ , all  $\tilde{Q}_\ell$  simultaneously jump to the same  $\phi_J$ , with the jammed structure dominated mainly by SS and SL. The results have shown that the evolution of both first and second jamming transitions is accompanied by a structural change in the system, where some HCP/FCC structures of large and small particles are formed.

The analysis of the structure factor has shown that the packing structures for  $\delta = 0.73$  are similar showing with approximately the same  $\phi_J$  as  $X_S$  changes. Although, each configuration type contributes differently to the total  $S(q)$ . Therefore, the jammed structures can be expected to be structurally similar for  $\delta = 0.73$ , regardless of the concentration of the small particles. Such an equivalence of packing structures needs to be confirmed and explained in future research.

We have also shown that the  $S(q)$  immediately before jamming is identical to the  $S(q)$  at jamming. This means that  $S(q)$  cannot distinguish whether the system is jammed or not. Choosing a variable that responds to each transition is important for understanding how jammed structures arise and which contact configuration contributes the most. The introduction of the contact orientational order aims to shed light on the local structures of the packings. Looking at the partial  $\tilde{Q}_\ell$ , one can determine how the contact configurations are packed when  $\phi \rightarrow \phi_J$ . This result could be crucial to understand how the strength of the bidisperse packing evolves. For example, it is of great importance to know how the bulk modulus and other macroscopic properties of the packings depend on the packing structure. The structural features presented here are consistent with the jamming density and bulk modulus reported in Ref. [15] along the first and second jamming transition, which can suggest a possible connection between them. In particular, the similar values of the jamming density and bulk modulus observed for  $\delta = 0.73$  may be due to the formation of equivalent jammed structures independent of  $X_S$ . For  $\delta = 0.15$ , the structures seem to correlate with the jamming density and bulk modulus, suggesting that the structure has an effect on them. Future work in this direction is ongoing.

---

### Acknowledgments

We thank Thomas Voigtmann, Philip Born, and Michael A. Klatt for proofreading and fruitful discussions. This work was supported by the German Academic Exchange Service (DAAD) under grant n<sup>o</sup> 57424730.

---

### Compliance with ethical standards

Conflict of Interest: The authors declare that they have no conflict of interest.

---

### References

- Aleksandar Donev, Salvatore Torquato, Frank H Stillinger, and Robert Connelly. Jamming in hard sphere and disk packings. *J. Appl. Phys.*, 95(3):989–999, 2004.
- C. S. O’Hern, L. E. Silbert, A. J. Liu, and S. R. Nagel. *Phys. Rev. E*, 68:011306, 2003.
- Leonardo E Silbert and Moises Silbert. Long-wavelength structural anomalies in jammed systems. *Phys. Rev. E*, 80(4):041304, 2009.
- T. S. Majmudar, M. Sperl, S. Luding, and R. P. Behringer. *Phys. Rev. Lett.*, 98:058001, 2007.
- Peter K Morse and Eric I Corwin. Geometric order parameters derived from the voronoi tessellation show signatures of the jamming transition. *Soft Matter*, 12(4):1248–1255, 2016.
- Ishan Prasad, Christian Santangelo, and Gregory Grason. Subjamming transition in binary sphere mixtures. *Phys. Rev. E*, 96(5):052905, 2017.
- Adam B Hopkins, Yang Jiao, Frank H Stillinger, and Salvatore Torquato. Phase diagram and structural diversity of the densest binary sphere packings. *Phys. Rev. Lett.*, 107(12):125501, 2011.
- Stefan Frank-Richter. PhD thesis, Universität Düsseldorf, 2014.
- Indaco Biazzo, Francesco Caltagirone, Giorgio Parisi, and Francesco Zamponi. Theory of amorphous packings of binary mixtures of hard spheres. *Phys. Rev. Lett.*, 102(19):195701, 2009.
- Salvatore Pillitteri, Geoffroy Lumay, Eric Opsomer, and Nicolas Vandewalle. From jamming to fast compaction dynamics in granular binary mixtures. *Sci. Rep.*, 9(1):7281, 2019.
- N. Kumar, V. Magnanimo, M. Ramaioli, and S. Luding. Tuning the bulk properties of bidisperse granular mixtures by small amount of fines. *Powder Technol.*, 293:94–112, 2016.
- Yusuke Hara, Hideyuki Mizuno, and Atsushi Ikeda. Phase transition in the binary mixture of jammed particles with large size dispersity. *Phys. Rev. Res.*, 3(2):023091, 2021.
- DJ Koeze, D Vågberg, BBT Tjoa, and BP Tighe. Mapping the jamming transition of bidisperse mixtures. *EPL*, 113(5):54001, 2016.
- Juan C Petit, Nishant Kumar, Stefan Luding, and Matthias Sperl. Additional transition line in jammed asymmetric bidisperse granular packings. *Phys. Rev. Lett.*, 125(21):215501, 2020.
- Juan C Petit, Nishant Kumar, Stefan Luding, and Matthias Sperl. Bulk modulus along jamming transition lines of bidisperse granular packings. *Phys. Rev. E*, 106(5):054903, 2022.
- R.J. Farris. Prediction of the viscosity of multimodal suspensions from unimodal viscosity data. *Trans. Soc. Rheol.*, 12(2):281–301, 1968.
- Andrew P. Shapiro and Ronald F. Probst. Random packings of spheres and fluidity limits of monodisperse and bidisperse suspensions. *Phys. Rev. Lett.*, 68(9):1422, 1992.
- Sidhant Pednekar, Jaehun Chun, and Jeffrey F. Morris. Bidisperse and polydisperse suspension rheology at large solid fraction. *J. Rheol.*, 62(2):513–526, 2018.
- Da He and Ndy N. Ekere. Viscosity of concentrated noncolloidal bidisperse suspensions. *Rheo. acta*, 40(6):591–598, 2001.
- Philippe Gondret and Luc Petit. Dynamic viscosity of macroscopic suspensions of bimodal sized solid spheres. *J. Rheol.*, 41(6):1261–1274, 1997.

- 
21. Andrew S. Clarke and Hannes Jónsson. Structural changes accompanying densification of random hard-sphere packings. *Phys. Rev. E*, 47(6):3975, 1993.
  22. Boris A Klumov, SA Khrapak, and GE Morfill. Structural properties of dense hard sphere packings. *Phys. Rev. B*, 83(18):184105, 2011.
  23. Boris A Klumov, Yuliang Jin, and Hernán A Makse. Structural properties of dense hard sphere packings. *J. Phys. Chem. B*, 118(36):10761–10766, 2014.
  24. M Hanifpour, Nicolas Francois, Vanessa Robins, Andrew Kingston, SM Vaez Allaei, and Mohammad Saadatfar. Structural and mechanical features of the order-disorder transition in experimental hard-sphere packings. *Phys. Rev. E*, 91(6):062202, 2015.
  25. See the webpage: [www.mercurydpm.org](http://www.mercurydpm.org).
  26. Thomas Weinhart, Luca Orefice, Mitchel Post, Marnix P van Schroyensteen Lantman, Irana FC Denissen, Deepak R Tunuguntla, JMF Tsang, Hongyang Cheng, Mohamad Yousef Shaheen, Hao Shi, et al. Fast, flexible particle simulations—an introduction to mercurydpm. *Computer physics communications*, 249:107129, 2020.
  27. Peter A Cundall and Otto DL Strack. A discrete numerical model for granular assemblies. *Géotechnique*, 29(1):47–65, 1979.
  28. Juan C Petit, Xavier García, Iván Sánchez, and Ernesto Medina. Contact angle entropy and macroscopic friction in noncohesive two-dimensional granular packings. *Phys. Rev. E*, 96(1):012902, 2017.
  29. Juan C Petit and Ernesto Medina. Reduction of the bulk modulus with polydispersity in noncohesive granular solids. *Phys. Rev. E*, 98(2):022903, 2018.
  30. Aleksandar Donev, Frank H Stillinger, and Salvatore Torquato. Do binary hard disks exhibit an ideal glass transition? *Phys. Rev. Lett.*, 96(22):225502, 2006.
  31. Pinaki Chaudhuri, Ludovic Berthier, and Srikanth Sastry. Jamming transitions in amorphous packings of frictionless spheres occur over a continuous range of volume fractions. *Phys. Rev. Lett.*, 104(16):165701, 2010.
  32. F. Göncü, O. Durán, and S. Luding. *C. R. Mécanique*, 338:570–586, 2010.
  33. CC Furnas. Grading aggregates-i.-mathematical relations for beds of broken solids of maximum density. *Ind. Eng. Chem. Res.*, 23(9):1052–1058, 1931.
  34. Ning Xu and Emily SC Ching. Effects of particle-size ratio on jamming of binary mixtures at zero temperature. *Soft Matter*, 6(13):2944–2948, 2010.
  35. Raphael Blumenfeld. Disorder criterion and explicit solution for the disc random packing problem. *Phys. Rev. Lett.*, 127(11):118002, 2021.
  36. Paul J Steinhardt, David R Nelson, and Marco Ronchetti. Bond-orientational order in liquids and glasses. *Phys. Rev. B*, 28(2):784, 1983.
  37. Anuraag R Kansal, Salvatore Torquato, and Frank H Stillinger. Diversity of order and densities in jammed hard-particle packings. *Phys. Rev. E*, 66(4):041109, 2002.
  38. CL Martin and RK Bordia. Influence of adhesion and friction on the geometry of packings of spherical particles. *Phys. Rev. E*, 77(3):031307, 2008.
  39. Nathan Duff and Daniel J Lacks. Shear-induced crystallization in jammed systems. *Phys. Rev. E*, 75(3):031501, 2007.
  40. Steven Fortune. Voronoi diagrams and delaunay triangulations. *Computing in Euclidean geometry*, pages 225–265, 1995.
  41. Walter Mickel, Sebastian C Kapfer, Gerd E Schröder-Turk, and Klaus Mecke. Shortcomings of the bond orientational order parameters for the analysis of disordered particulate matter. *Chem. Phys.*, 138(4):044501, 2013.
  42. Jan Haeberle, Matthias Sperl, and Philip Born. Distinguishing noisy crystalline structures using bond orientational order parameters. *Eur. Phys. J. E*, 42(11):1–7, 2019.
  43. Hideyuki Mizuno, Kuniyasu Saitoh, and Leonardo E Silbert. Structural and mechanical characteristics of sphere packings near the jamming transition: From fully amorphous to quasiordered structures. *Phys. Rev. Mater.*, 4(11):115602, 2020.